International Journal of Basic and Applied Sciences, 14 (2) (2025) 551-562

International Journal of Basic and Applied Sciences

Website: www.sciencepubco.com/index.php/IJBAS
https://doi.org/10.14419/fwcbdd76
Research paper

Integrated Antenna Design with SAW Filters

K. R. Saranya [1], D. Kalaiyarasi [2], D. Sugumar [3], Jeba Johannah J. [4], S. Dhivya [5], Subramanyam Kunisetti [6], A. Thilagavathy [7], T. V. V. Satyanarayana [8] *

[1] *Department of Computer Science and Engineering, School of Computing, SRM Institute of Science and Technology, Tiruchirapalli, Tamil Nadu 621105, India*
[2] *Department of Electronics and Communication Engineering, Panimalar Engineering College, Chennai, Tamil Nadu 600123, India*
[3] *Department of Electronics and Communication Engineering, Karunya Institute of Technology and Sciences (Deemed to be a University), Coimbatore, Tamil Nadu 641114, India*
[4] *Department of Electronics and Communication Engineering, St. Joseph's Institute of Technology, Chennai, Tamil Nadu 600119, India*
[5] *Department of Research and Innovation, Saveetha School of Engineering, SIMATS, Chennai, Tamil Nadu 602105, India*
[6] *Department of Computer Science and Engineering (Data Science), R.V.R. & J.C. College of Engineering, Guntur, Andhra Pradesh 522019, India*
[7] *Department of Computer Science and Engineering, R.M.K. Engineering College, Kavaraipettai, Tamil Nadu 601206, India*
[8] *Department of Electronics and Communication Engineering, School of Engineering, Mohan Babu University, Tirupati, Andhra Pradesh 517102, India*
**Corresponding author E-mail: saranya.kr@ist.srmtrichy.edu.in*

Received: May 11, 2025, Accepted: June 18, 2025, Published: June 30, 2025

Abstract

This work presents the design, simulation, and fabrication of a branch-and-leaf fractal Antipodal Vivaldi antenna, demonstrating a 60% size reduction compared to a conventional counterpart. Despite a 15% decrease in radiation characteristics, the antenna satisfies the ultra-wideband (UWB) requirements essential for applications such as ground-penetrating radar (GPR) systems used in humanitarian demining in Colombia. The enhanced performance is attributed to the additional resonant modes introduced by the fractal geometry, which increases gain across multiple frequencies. The resulting miniaturization facilitates a reduced form factor for GPR systems, improving field deployment and operational efficiency. Future work includes a parametric study of alternative fractal geometries, such as Minkowski Island designs, to further optimize performance and integration into advanced field measurement systems for sustained demining operations.

Keywords: *Fractal Antenna; Ultra-Wideband (UWB); Antipodal Vivaldi Antenna; Ground-Penetrating Radar (GPR); Humanitarian Demining.*

1. Introduction

Humanitarian demining is a problem that affects not only countries with mines but also countries around the world. As of 2017, 162 countries have signed the Mine Ban Treaty, in which they commit, among other things, to clear all mined areas within their territory within 10 years (Hsu, Tseng, & Li, 2021, Xu et al., 2022, Shen et al., 2021a, Ren, Xu, Le, & Lee, 2021). Various systems have been used in the demining process, including systems such as subsurface metal detection and ground-penetrating radar (GPR).
For this document, the GPR system is of great interest, as the antennas designed here correspond to the parameters required by a GPR. Within the framework of the development of GPR antennas for humanitarian demining, Vivaldi antennas can provide a portable and precise solution to this global problem (Butaud et al., 2020; Xu et al., 2021; Su et al., 2021a).
For this document, Vivaldi antennas are of particular interest due to their wide frequency response. In addition, fractal designs found in nature provide the basis for this work to modify a conventional Vivaldi Antipodal antenna to improve its efficiency and reduce its size (Su et al., 2022; Kadota & Tanaka, 2018; Hsu, Tseng, & Li, 2020).
This document reports the design and simulation stages of three different antennas, reported by (Su et al., 2021b; Zhang et al., 2020; Shen et al., 2022), to verify the improvement in efficiency and radiation of each antenna compared to the previous one.
As a final procedure, the final antenna will be printed for testing and proper operation of the elements. Thus, the document presented here is structured as follows (Figures 1- 3):

- Conventional Vivaldi Antipodal Antenna

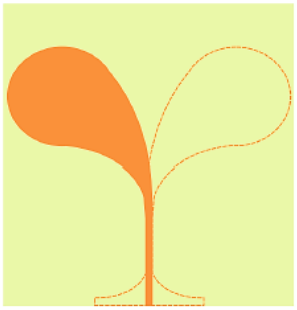

Fig. 1: Conventional Vivaldi Antipodal Antenna.

- Branch Vivaldi Antipodal Antenna

Fig. 2: Branch Vivaldi Antipodal Antenna.

- Branch and Leaf Vivaldi Antipodal Antenna

Fig. 3: Vivaldi Antipodal Antenna of Branches and Leaves.

2. Literature review

Bahamonde & Kymissis (2020) present a reconfigurable SAW filter implemented on a ZnO/AlGaN/GaN heterostructure, which enables tunability in frequency response. This is achieved through the application of an electric field, influencing the piezoelectric properties of ZnO. The relevance of this work lies in demonstrating integration potential with high-electron-mobility devices and compact, tunable architectures, crucial for miniaturized RF modules.

Azarnaminy et al. (2021) explore a dual-band SAW filter with integrated vanadium oxide switches. These switches enable frequency reconfiguration, allowing for dynamic dual-band operation. The innovation here is the use of VO_2, a phase-change material, as a switching mechanism, contributing to filter adaptability in modern RF front-ends.

Yang et al. (2021) propose a miniaturized dual-band bandpass filter using thin-film lithium niobate. The design exploits acoustic mode coupling for size reduction and achieves strong band isolation. The significance lies in demonstrating how thin-film acoustic technologies can achieve high performance with reduced size, supporting compact multiband wireless systems.

Luo et al. (2022) detail the design and optimization of a dual-mode Lamb wave resonator, forming a dual-passband filter. Using FEM simulations, they optimize electrode design and layer structures to simultaneously excite two Lamb wave modes. This design achieves high Q-factors and dual-band response, relevant for dual-band GPR front-end systems requiring tight spectral control.

Zou et al. (2020) introduce a dual-mode thin-film bulk acoustic wave resonator (FBAR) and demonstrate its filtering capabilities. By carefully engineering the acoustic stack, they achieve effective dual-mode operation, providing compactness and high selectivity. Their results show FBAR potential in UWB contexts where precise band allocation is needed.

Phani Kumar et al. (2021) present a microstrip dual-band bandpass filter fabricated on a paper substrate. This eco-friendly approach maintains performance while offering a sustainable alternative to conventional substrates. The wide bandwidth and dual-band nature of this design are directly applicable to low-cost, deployable GPR devices, particularly in humanitarian contexts where disposability and environmental safety are factors.

Acosta et al. (2022) provide a topological analysis of dual-band filters based on acoustic resonators. The paper categorizes multiple resonator configurations and evaluates their frequency responses, compactness, and performance metrics. This comprehensive analysis aids in selecting optimal geometries for size-sensitive applications, like portable GPR units.

Campanella et al. (2021) introduce a monolithic multiband MEMS RF front-end module tailored for 5G mobile applications. This integrated system combines MEMS switches with acoustic filters, achieving multiband functionality in a compact package. Their work is instructive for the integration of antenna systems with reconfigurable and miniaturized filtering architectures.
Liu et al. (2020) review the materials, design methodologies, and characteristics of bulk acoustic wave (BAW) resonators. This review highlights material selection, acoustic confinement techniques, and thermal stability—key considerations when adapting resonator technologies for extreme or field-based applications such as demining.
Campanella et al. (2020) highlight the strategic importance of ambidextrous organizations in the banking sector, showing that the ability to balance exploration and exploitation can improve performance in dynamic financial environments. In the field of antenna engineering, Hanna and Sharma (2016) provide a review of fractal antenna geometries, highlighting their advantages in miniaturization, multiband functionality, and better bandwidth availability—these include stronger pulse-to-groundbandwidth, such as pulpwindtrap).
Meanwhile, Babu et al. (2022) investigate the integration of machine learning in predictive multiscale design and additive manufacturing, showing that data-driven models can accelerate material and structural optimization, reduce production time, and improve design accuracy. Based on the interdisciplinary developments reviewed in the literature, ranging from intelligent traffic systems to machine learning-based manufacturing, design and optimization play a key role in many fields. Based on this premise, the following section describes the methodology used to design and 3D model the antenna structures. This methodological framework integrates key principles from previous research to guide the practical implementation of the design while maintaining functional efficiency and structural integrity.

3. 3D design and modeling

Building on the insights from the literature—particularly the emphasis on innovation in design and optimization—the following section outlines the practical methodology adopted for 3D modeling of the proposed antenna structures.

3.1. Procedure

The 3D model design procedure was the same for each of the antennas analyzed. Due to the intricate structure of the fractal antennas studied, it was necessary to use an alternative surface design tool. The design GUI integrated into the HFSS simulation software contains basic tools that allow the generation of antenna models similar to the conventional antipodal Vivaldi antenna analyzed in this document, but it is not suitable for complex designs requiring extensive structural work, such as the fractal antennas reported here.
The program used was InkScape, a software that generates .dxf files that can be imported into HFSS as surfaces. To better understand the design process for the antennas of interest, the following flowchart of Figure 4 is presented:

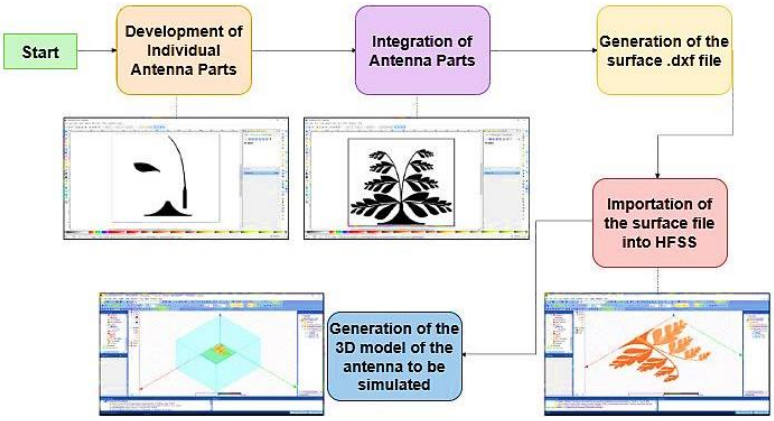

Fig. 4: Modeling Procedure for the Antennas to Be Analyzed.

3.2. Conventional Vivaldi antipodal antenna

The design and modeling of the conventional Vivaldi Antipodal antenna is of great interest because it will be used as a control test to verify the efficiency and radiation improvements of the Vivaldi Antipodal Branch Antenna and the Vivaldi Antipodal Branch and Leaf Antenna. The design and modeling results of the conventional Vivaldi Antipodal antenna are as shown in Figure 5:

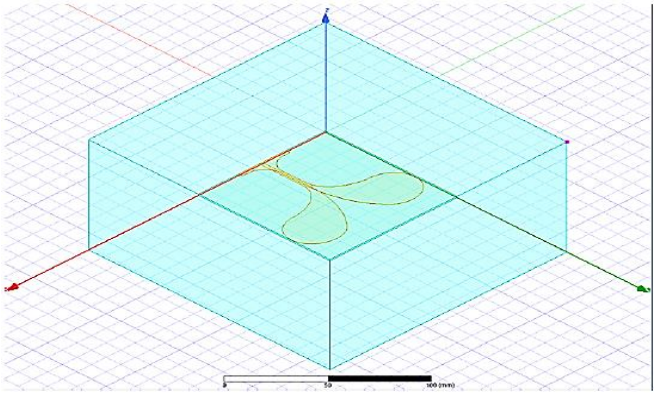

Fig. 5: Modeling of the Conventional Vivaldi Antipodal Antenna.

3.3. Vivaldi antipodal branch antenna

The design and modeling of the Vivaldi Antipodal Branch Antenna is the first fractalization iteration performed on the antennas analyzed. The design and modeling results of the Vivaldi Antipodal Branch Antenna are as in Figure 6:

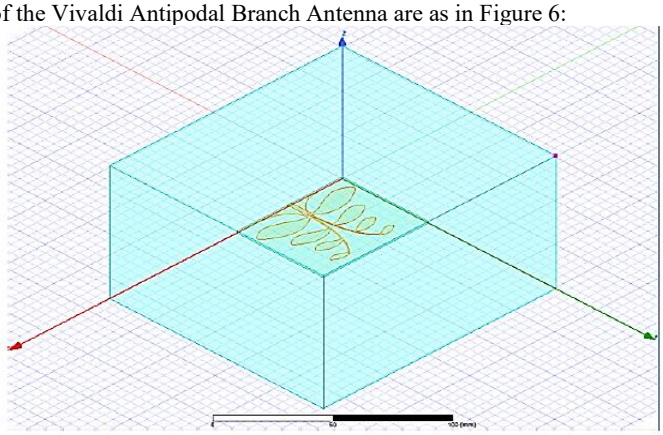

Fig. 6: Modeling of the Conventional Vivaldi Antipodal Antenna.

3.4. Vivaldi antipodal branch-and-leaf antenna

The design and modeling of the Vivaldi Antipodal Branch-and-Leaf Antenna is the most relevant design of this work, being the second fractalization iteration studied.
The design and modeling result of the Vivaldi Antipodal Branch Antenna is as as in Figure 7:

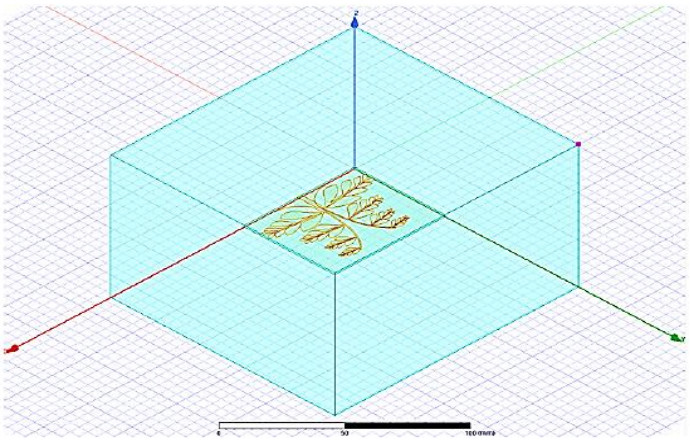

Fig. 7: Modeling of the Conventional Vivaldi Antipodal Antenna.

4. Simulation

With the antenna structures accurately modeled, the next phase involved simulating their electromagnetic performance to validate the design objectives and compare behavior across configurations.

4.1. Procedure and generated results

After the antenna modeling stage, the simulation of their parameters was carried out. The results generated were as follows:

- Reflection parameter (S11).
- Gain vs. Frequency.
- Radiation Patterns (2 GHz, 7 GHz, 12 GHz, 20 GHz / E-Plane, H-Plane)

Some of the most important initialization elements for each simulation were:

- Radiation Box: A radiation box was used at $\lambda/4$ from the simulated antenna surface. This is because the HFSS simulation attempts to mimic the operation of a real anechoic chamber. To achieve this, the distance between the radiating object and the radiation box must be at least $\lambda/4$ (λ being the minimum simulation frequency: 2 GHz). This $\lambda/4$ distance is used because similar impedance mismatches can cancel out within a quarter of a wavelength, ensuring that no reflected waves are reflected, and the boundary of the radiation box absorbs all reflections.
- Simulation Mode: A discrete simulation mode was used so that all radiation characteristics could be saved: radiation pattern graphs at the frequencies of interest, multi-frequency surface current distribution graphs, and finally, reflection parameter and gain vs. frequency results.

The results obtained are presented below, along with the corresponding reference (indexed in IEEE documents), which validates the correct generation of each of the parameters of interest.

4.2. Results and validation

4.2.1. Conventional Vivaldi antipodal antenna

- Reflection parameter

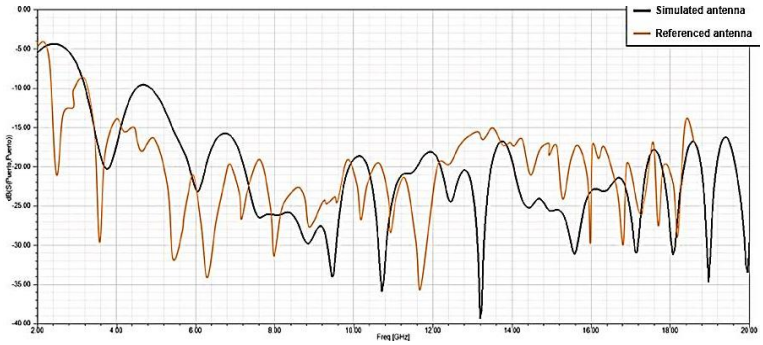

Fig. 8: Reflection Parameter of the Conventional Vivaldi Antipodal Antenna and the Conventional Vivaldi Antipodal Antenna.

As can be seen in Figure 8, the S11 parameter of the conventional Vivaldi Antipodal antenna mostly matches the desired performance of the Vivaldi Antipodal antenna designed by Su et al. (2022), designed for broadband operation from 2 GHz to 18 GHz.

- Gain

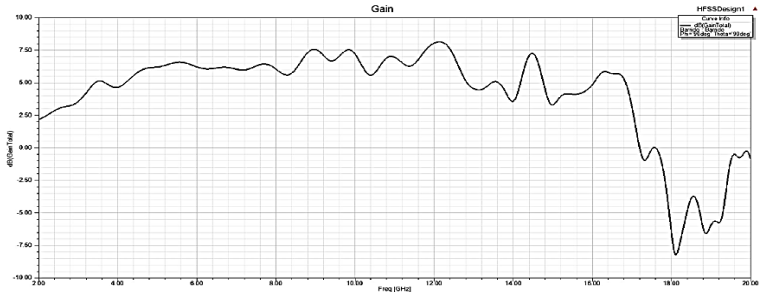

Fig. 9: Gain vs. Frequency of the Conventional Vivaldi Antipodal Antenna.

In this section, it can be seen in Figure 9 that the maximum gain of the simulated conventional Vivaldi Antipodal antenna is 7.5 dB.

- Radiation Patterns

The radiation patterns at 2 GHz, 7 GHz, 12 GHz, and 20 GHz demonstrate the frequency-dependent behavior of the designed fractal Antipodal Vivaldi antenna. As expected in ultra-wideband (UWB) systems, the radiation characteristics evolve with frequency due to the complex current distribution influenced by the fractal geometry. Figure 10, which shows the radiation patterns of the fractal antenna at 2 GHz, 7 GHz, 12 GHz, and 20 GHz:

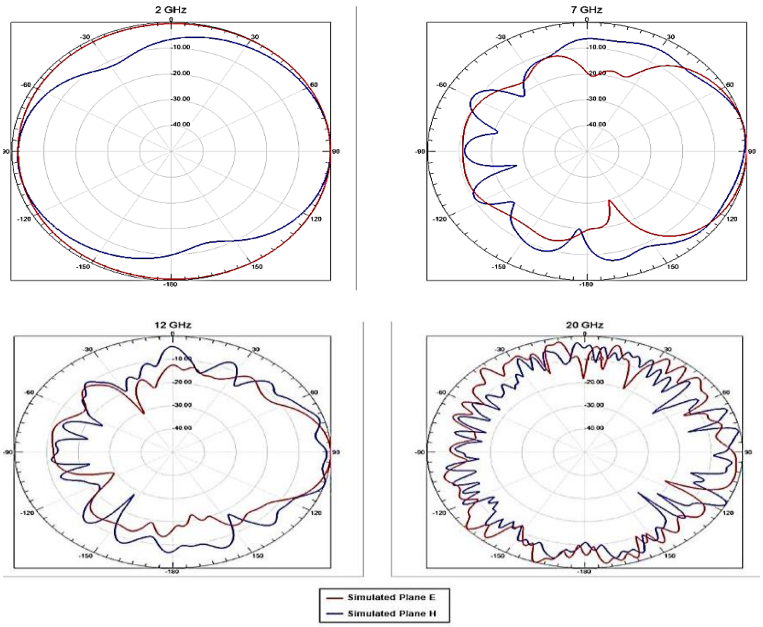

Fig. 10: Radiation Patterns at 2 GHz, 7 GHz, 12 GHz, and 20 GHz, Respectively.

To validate the correct operation of the radiation patterns generated for this antenna, an additional pattern was created at 16 GHz that was comparable to the reference (Su et al., 2022). Figure 11 illustrates the radiation characteristics of the proposed fractal antenna at 16 GHz, plotted in both the E-plane (elevation) and H-plane (azimuth), and compares them to the performance of a conventional design reported in (Su et al., 2022).

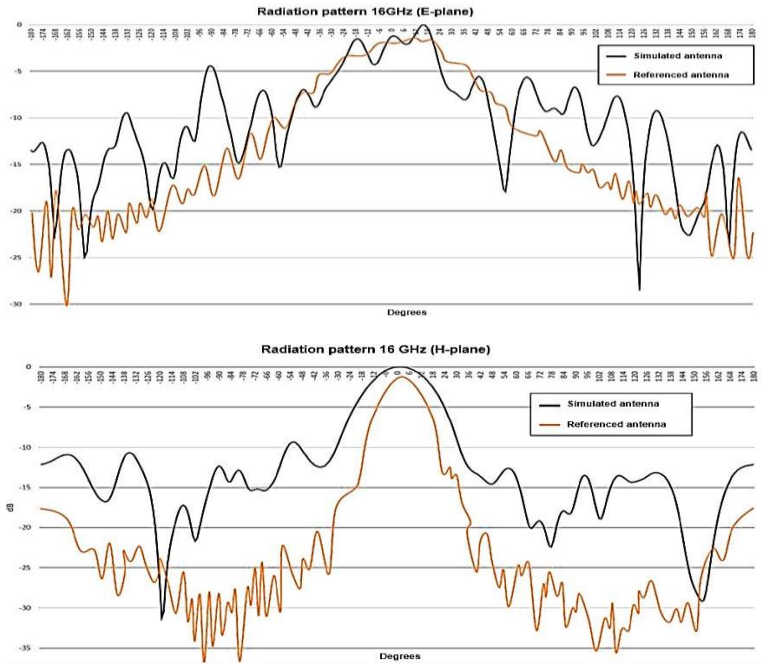

Fig. 11: Radiation Pattern at 16 GHz in the E and H Planes Compared to (Su et al., 2022).

As can be seen, the behavior of both radiation patterns, the simulation and the reference, is similar, thus validating the correct simulation of the conventional Vivaldi Antipodal Antenna.

4.2.2. Branch Vivaldi Antipodal Antenna

- Reflection parameter

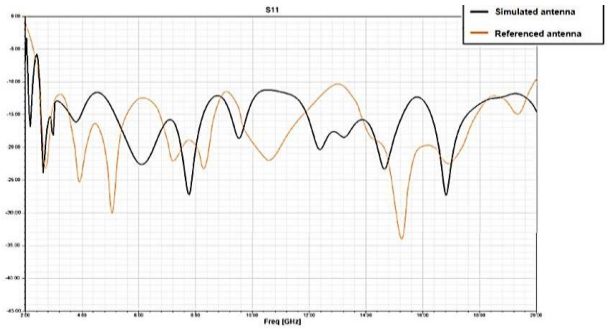

Fig. 12: Reflection Parameter of the Vivaldi Antipodal Branch Antenna and the Vivaldi Antipodal Branch Antenna in (Xu Et Al., 2022).

As can be seen in Figure 12, the S11 parameter of the Vivaldi Antipodal Branch Antenna mostly matches the desired behavior of the Vivaldi Antipodal Antenna designed by B. Biswas, R. Ghatak, and D. R. Poddar in (Xu et al., 2022).

- Gain

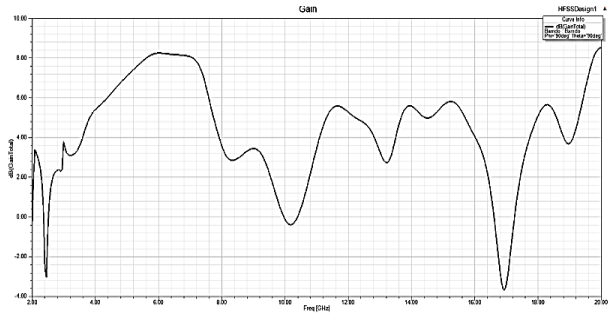

Fig. 13: Gain vs. Frequency of the Vivaldi Antipodal Branch Antenna.

In this section, it can be seen in Figure 13 that the maximum gain of the simulated Vivaldi Antipodal Branch Antenna is 8.1 dB.

- Radiation Patterns

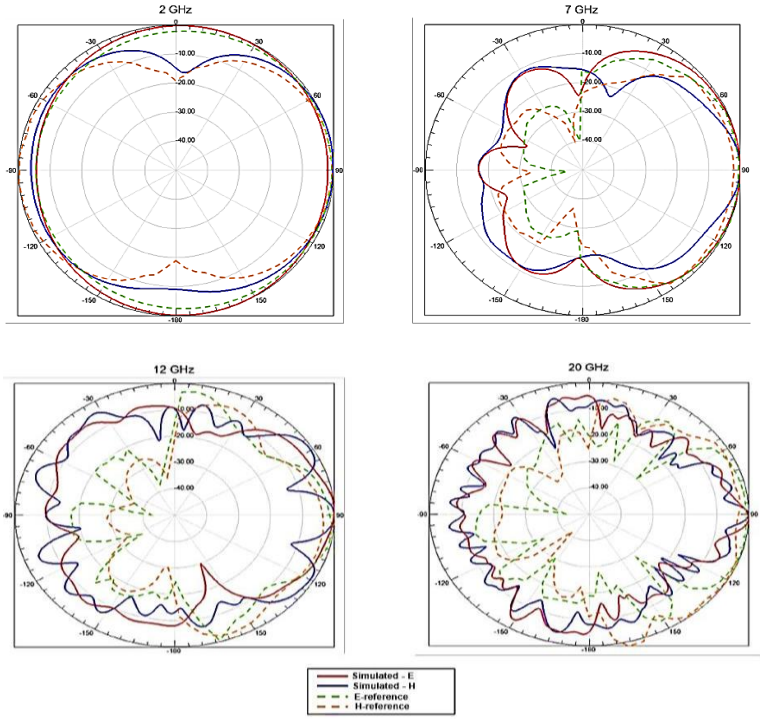

Fig. 14: Radiation Patterns at 2 GHz, 7 GHz, 12 GHz, and 20 GHz, Respectively.

As can be seen in Figure 14, the behavior of both radiation patterns, the simulation and the reference (Xu et al., 2022), are similar, thus validating the correct simulation of the Vivaldi Antipodal Branch Antenna.

4.2.3. Vivaldi antipodal branch-leaf antenna

- Reflection Parameter

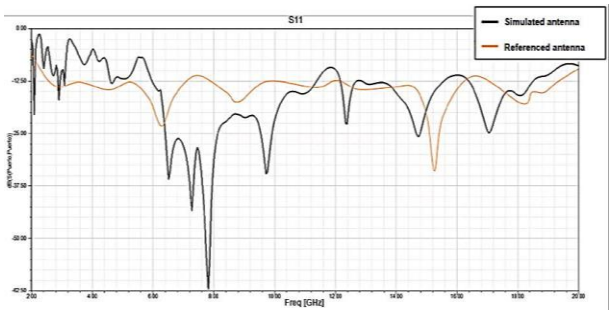

Fig. 15: Reflection Parameter of the Vivaldi Antipodal Branch-Leaf Antenna and the Vivaldi Antipodal Branch-Leaf Antenna in (Xu et al., 2022).

As can be seen in Figure 15, the S11 parameter of the Vivaldi Antipodal Branch-and-Leaf Antenna mostly matches the desired behavior of the Vivaldi Antipodal Antenna designed by Xu et al., 2022).

- Gain

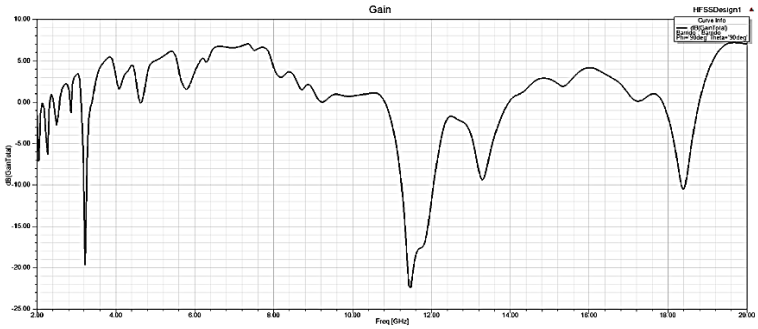

Fig. 16: Gain vs. Frequency of the Vivaldi Antipodal Branch-and-Leaf Antenna.

In this section in Figure 16, the maximum gain of the simulated Vivaldi Antipodal Branch-and-Leaf Antenna is 7.1 dB.

- Radiation Patterns

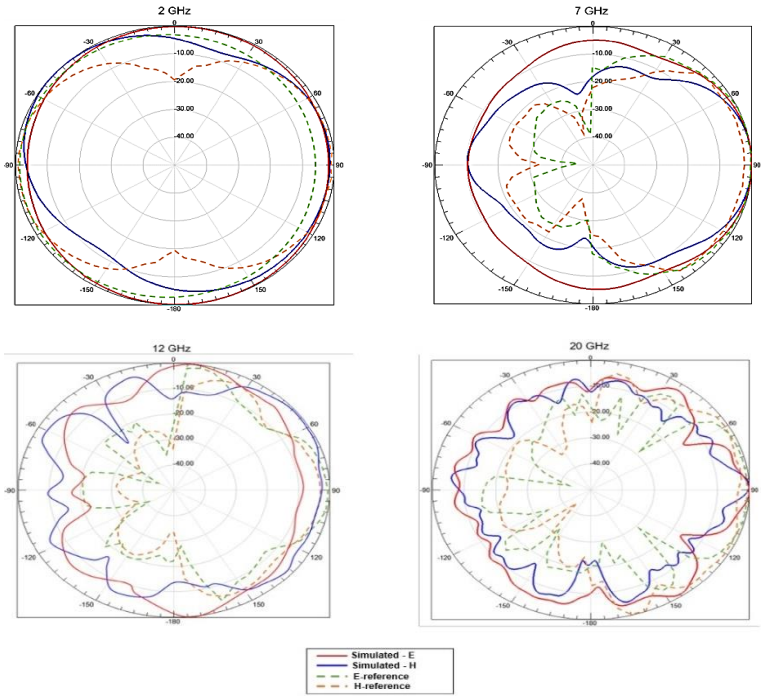

Fig. 17: Radiation Patterns at 2 GHz, 7 GHz, 12 GHz, and 20 GHz, Respectively.

As can be seen in Figure 17, the behavior of both radiation patterns, the simulation and the reference (Xu et al., 2022), are similar, thus validating the correct simulation of the Vivaldi Antipodal Branch-and-Leaf Antenna.

5. Anechoic chamber tests

Having confirmed the antenna's performance through simulation, the next phase involved experimental validation through physical prototyping and measurement in a controlled environment.

5.1. Prototype printing

To print the prototype (Vivaldi Antipodal Branch and Leaf Antenna), DipTrace, a freely available Gerber file generation software, was used. The program allows surfaces to be entered in the same format as generated by the software used for surface generation.
Subsequently, the necessary Gerber files (Top, Bottom, DRL) were generated and sent to the printed circuit board laboratory at the Universidad de los Andes. After 3 days, the prototype was finished, SMA-type connections were soldered to the board, and the final device obtained was as in Figure 18.

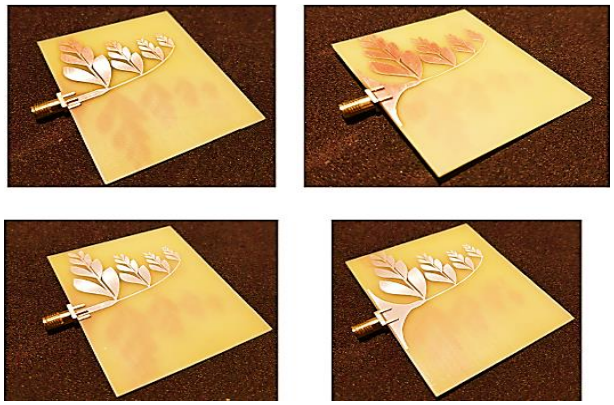

Fig. 18: Prototype Generated with A Copper Layer and A Tinned Copper Layer.

Two types of layers were printed because the copper layer oxidizes very easily, which can affect the readings taken in the anechoic chamber.

6. Results and validation

For measurement purposes, the anechoic chamber was used for a total of 3 hours, and the generated prototype underwent the necessary tests to obtain the S11 reflection pattern, the gain, and finally the radiation patterns for each of the frequencies of interest.

- Reflection parameter

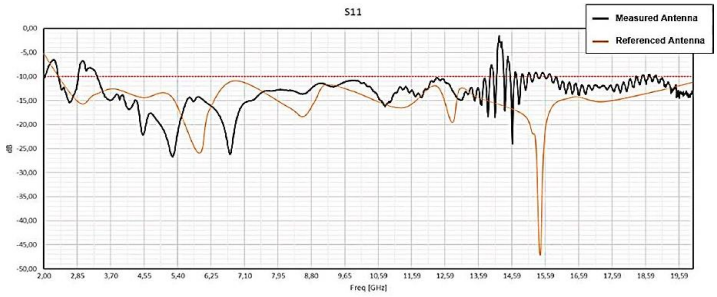

Fig. 19: Reflection Parameter of the Prototype Antenna.

As can be seen in Figure 19, the S11 parameter of the prototype antenna mostly matches the performance sought in the printed antenna by Xu et al., 2022).

- Radiation patterns

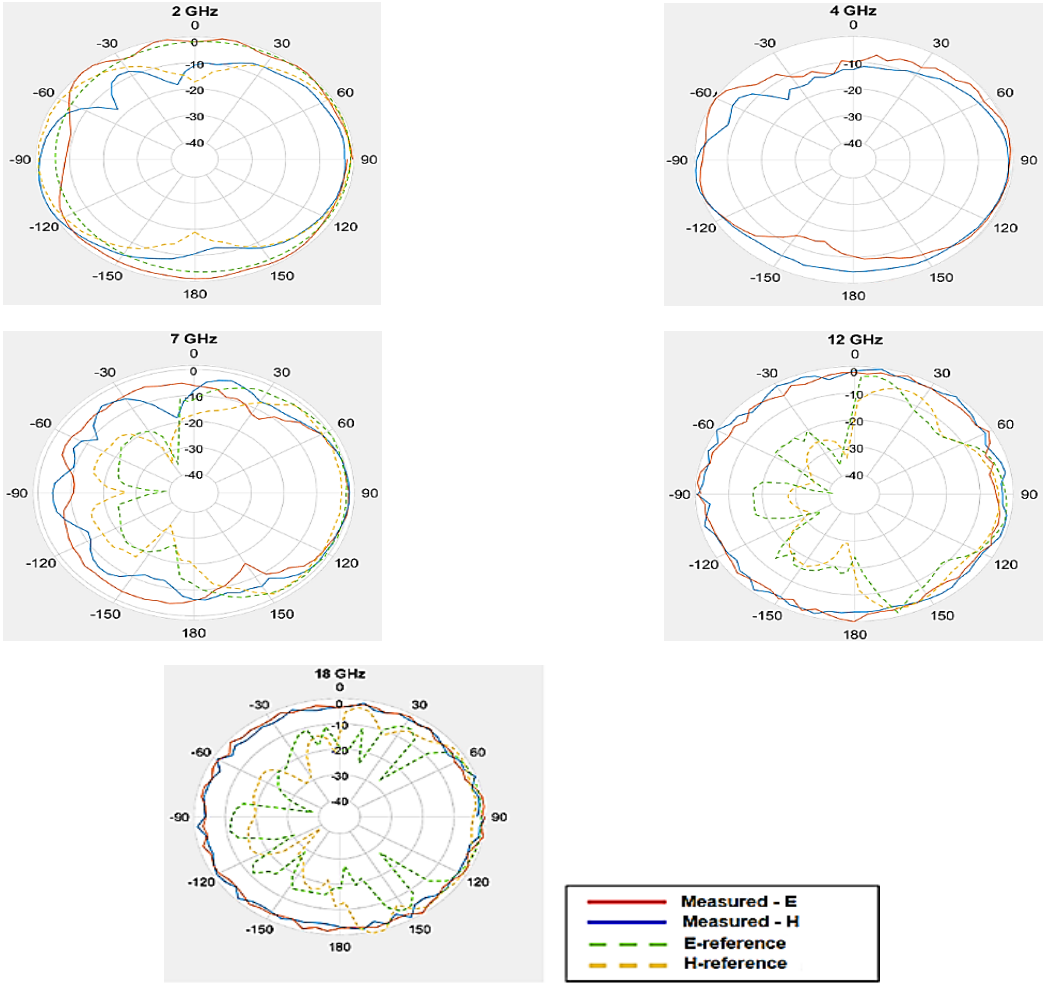

Fig. 20: Radiation Patterns at 2 GHz, 7 GHz, 12 GHz, and 20 GHz, Respectively.

As can be seen in both Figure 19 and Figure 20, starting at approximately 12 GHz, an unexpected effect appears on both the S11 parameter and the radiation patterns for 12 GHz and 18 GHz. This may be due to the anechoic chamber's operating preset, the multiple splicing of metallic materials in the antenna (copper, tin, lead particles, iridescent copper, SMA connector dielectric, etc.), and other effects that can induce noise or unwanted readings at high frequencies.

- Gain

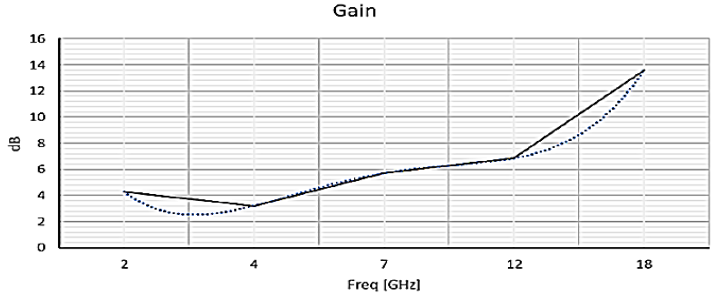

Fig. 21: Gain vs. Frequency of the Prototype Antenna.

In this section, it can be seen in Figure 21 that the maximum gain of the simulated conventional Vivaldi Antipodal antenna is 13.5 dB. As can be seen, the graph consists of a few points because the gain value was taken only for the frequencies of interest measured in the anechoic chamber (2 GHz, 4 GHz, 7 GHz, 12 GHz, 18 GHz).

7. Analysis

Building upon the simulated gain results, a deeper understanding of the antennas' performance can be gained through electromagnetic field distribution analysis, particularly surface current behavior and radiation characteristics.

7.1. Surface current and radiation analysis

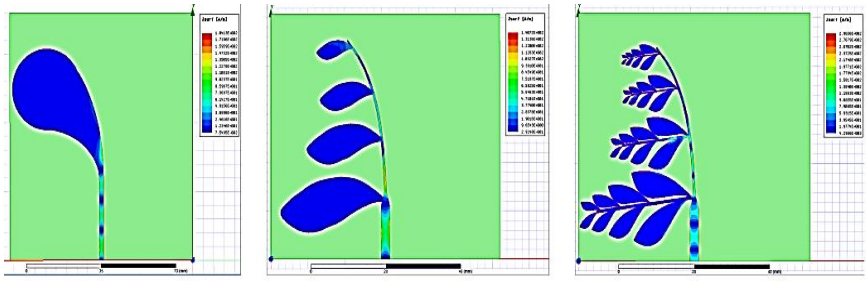

a b c

Fig. 22: Surface Current Distribution At 7 GHz for the Three Types of Simulated Antennas (Conventional Vivaldi Antipodal Antenna (A), Branch Antenna (B), And Branch and Leaf Antenna (C).

As can be seen in Figure 22, the surface currents of the different simulated antennas at 7 GHz are presented. It is easily noticeable in the different leaves of Figure 22a that the broadband characteristics of the antennas result from surface currents along the edges of the leaves, where the antennas themselves acquire additional resonances. This effect is also evident in the upper part of the antenna in Figure 22b, which can be seen by zooming in on Figure 22b.
The increase in bandwidth is due to the accumulation of charge in certain regions of the leaves or branches of each antenna, which explains their performance. broadband due to the length of the fractalization itself.
Similarly, Figure 23 shows that surface currents are mostly concentrated in the lower region of the antennas, the feed line.

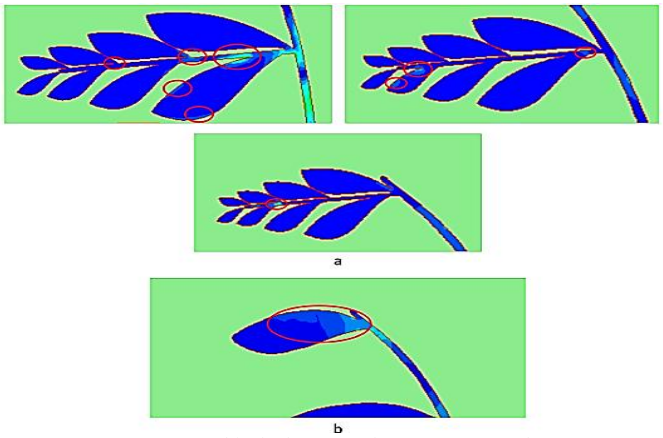

a

b

Fig. 23: Graphical Close-Up of Images 6.1 B and C.

Regarding the radiation characteristics, similar to the report in (Hsu, Tseng, & Li, 2020), the characterized antennas are of the Vivaldi Antipodal type, with slightly directional radiation patterns at low frequencies and increasing directivity in the direction of the upper radiating boundary with increasing frequency (refer to sections 4 and 5, Radiation Patterns). This general behavior is not fully visible in Figure 20 at the 12 GHz and 20 GHz frequencies, for the reasons discussed in that section.
As shown in Figure 20, at frequencies above 12 GHz, especially at 12 GHz and 18 GHz, an unexpected change is observed in the performance of the radiation pattern. Similarly, the influence parameter (S11) in Figure 19 shows signs of bias in this higher frequency range. These anomalies can be caused by a variety of factors. One of the main issues is the combination of different metallic materials—for example, copper, tin, and solder joints—which can cause surface impedance distortion due to the skin effect, which is more pronounced at higher frequencies. In addition, the SMA connectors used may not be fully tuned for millimeter wave operation, resulting in inconsistent losses. The dielectric properties of substrates and interlayers can introduce dispersion or resonance effects that alter the electromagnetic behavior beyond 12 GHz. In addition, anechoic chamber limitations, such as reduced absorber performance at higher frequencies or calibration inaccuracies, may contribute to measurement noise or pattern variation. To address these issues, several strategies have been recommended: using uniform materials with lower impedances, using precise connectors designed for frequencies up to or above 20 GHz, and optimizing the PCB layout to reduce interference. Camera-related errors can be reduced by calibrating equipment specifically for high-frequency bands, using finer angular resolution during pattern capture, and validating measurements with other techniques, such as time-domain measurements or network embeddings. The incorporation of surface acoustic wave (SAW) filters can help remove unwanted spectral components and improve signal purity during post-processing.

7.2. Comparative analysis of the simulated antennas

Table 1: Performance Comparison Before and After SMOTE Application (Test 2 - Precision)

Antenna	Size [mm]	Gain [dB]	Design	BW [GHz]
Vivaldi Antipodal conventional	90 x 87 x 1	7.5	Simple	17.75
Vivaldi Antipodal branch	50.8 x 62 x 1	8.1	Complex	14
Vivaldi Antipodal branch and leaf	50.8 x 62 x 1	13	Complex	14.89

As can be seen in Table 1, the fractalization of the conventional Antipodal Vivaldi Antenna results in a 60% size reduction, without losing radiation properties and with a 15% BW reduction. This corroborates the main principle of fractal antennas: Fractal antennas use a design similar to their generating geometries to maximize the length of the conductive material over a total surface area. This makes fractal antennas compact and broadband (Su et al., 2021b.

Table 2: Performance Comparison Before and After SMOTE Application (Test 2 - Precision)

Antenna Design	Type	Min S11 (dB)	Frequency @ Min S11 (GHz)	Bandwidth (GHz) Approx.	Peak Gain (dBi) Approx.
Vivaldi Antipodal Branch-and-Leaf	Simulated	–55	8.0	2.8 – 18.2	~5.5
	Referenced	–17	6.0	3.0 – 17.6	~5.0
Vivaldi Antipodal Branch	Simulated	–25	14.0	3.0 – 18.5	~6.0
	Referenced	–29	14.0	3.5 – 17.8	~5.8
Vivaldi Antipodal conventional	Simulated	–35	14.0	3.5 – 18.8	~6.5
	Referenced	–28	6.0	3.2 – 17.5	~6.0

The comparison shows that the compared antennas outperform the other antennas in all three designs. While the branch-leg design provides the best impedance matching (S11 of –55 dB) and wide bandwidth (2.8–18.2 GHz), the branch design shows equivalent performance with a moderate gain (~6.0 dBi) in the broad bandwidth. The conventional (Split-Ring) simulation antenna provides the highest gain (~6.5 dBi) and highest bandwidth (3.5–18.8 GHz), making it the most effective for UWB applications. Overall, the simulation improvements improve S11, bandwidth, and continuity across all models.

8. Conclusions and future work

As mentioned, fractal structures can successfully reduce the size of antennas without sacrificing performance. The branch-and-neck fractal antenna presented in this work achieved a loss of 60% compared to a conventional Antipodal Vivaldi antenna, with a radiation performance of only 15%—better addressing the ultra-wideband (UWB) requirements of GP systems with above-human applications. This miniaturization is due to the different resonant modes introduced by the fractal geometry, which increase the gain over a wide frequency range. Furthermore, the reduction of the form factor offers significant advantages for local-mobile GPR units, allowing for improved maneuverability in complex terrain.

For future work, consider co-designing or co-simulating the antenna and SAW filter as a single front-end system to enhance performance, reduce losses, and improve integration for compact GPR applications.

References

[1] Hsu, T. H., Tseng, K. J., & Li, M. H. (2021). Thin-film lithium niobate-on-insulator (LNOI) shear horizontal surface acoustic wave resonators. *Journal of Micromechanics and Microengineering, 31*(5), 054003. https://doi.org/10.1088/1361-6439/abf1b5.

[2] Xu, H., Fu, S., Shen, J., Lu, Z., Su, R., Wang, R., Song, C., Zeng, F., & Pan, F. (2022). Large-range spurious mode elimination for wideband SAW filters on $LiNbO_3/SiO_2/Si$ platform by $LiNbO_3$ cut angle modulation. *IEEE Transactions on Ultrasonics, Ferroelectrics, and Frequency Control, 69*(10), 3117–3125. https://doi.org/10.1109/TUFFC.2022.3152010.

[3] Shen, J., Fu, S., Su, R., Xu, H., Lu, Z., Xu, Z., Luo, J., Zeng, F., Song, C., Wang, W., et al. (2021). High-performance surface acoustic wave devices using $LiNbO_3/SiO_2/SiC$ multilayered substrates. *IEEE Transactions on Microwave Theory and Techniques, 69*(8), 3693–3705. https://doi.org/10.1109/TMTT.2021.3077261.

[4] Ren, Z., Xu, J., Le, X., & Lee, C. (2021). Heterogeneous wafer bonding technology and thin-film transfer technology-enabling platform for the next generation applications beyond 5G. *Micromachines, 12*(8), 946. https://doi.org/10.3390/mi12080946.

[5] Butaud, E., Tavel, B., Ballandras, S., Bousquet, M., Drouin, A., Huyet, I., Courjon, E., Ghorbel, A., Reinhardt, A., Clairet, A., et al. (2020). Smart CutTM Piezo on Insulator (POI) substrates for high performances SAW components. In *Proceedings of the 2020 IEEE International Ultrasonics Symposium (IUS)* (pp. 4–7). Las Vegas, NV, USA. https://doi.org/10.1109/IUS46767.2020.9251517.

[6] Xu, H., Fu, S., Su, R., Shen, J., Zeng, F., Song, C., & Pan, F. (2021). Enhanced coupling coefficient in dual-mode ZnO/SiC surface acoustic wave devices with partially etched piezoelectric layer. *Applied Sciences, 11*(14), 6383. https://doi.org/10.3390/app11146383.

[7] Su, R., Fu, S., Lu, Z., Shen, J., Xu, H., Mao, H., Xu, Z., Song, C., Zeng, F., & Wang, W., et al. (2021). Near 30% fractional bandwidth surface acoustic wave filters with novel electrode configuration. *Progress in Natural Science: Materials International, 31*(6), 852–857. https://doi.org/10.1016/j.pnsc.2021.08.001.

[8] Su, R., Fu, S., Lu, Z., Shen, J., Xu, H., Xu, Z., Wang, R., Song, C., Zeng, F., & Wang, W., et al. (2022). Over GHz bandwidth SAW filter based on 32° Y-X LN/SiO_2/poly-Si/Si heterostructure with multi-layer electrode modulation. *Applied Physics Letters, 120*(25), 253501. https://doi.org/10.1063/5.0092767.

[9] Kadota, M., & Tanaka, S. (2018). Wideband acoustic wave resonators composed of hetero acoustic layer structure. *Japanese Journal of Applied Physics, 57*(7), 07LD12. https://doi.org/10.7567/JJAP.57.07LD12.

[10] Hsu, T. H., Tseng, K. J., & Li, M. H. (2020). Large coupling acoustic wave resonators based on $LiNbO_3/SiO_2$/Si functional substrate. *IEEE Electron Device Letters, 41*(11), 1825–1828. https://doi.org/10.1109/LED.2020.3030797.

[11] Su, R., Shen, J., Lu, Z., Xu, H., Niu, Q., & Xu, Z. (2021). Wideband and low-loss surface acoustic wave filter based on 15° YX-$LiNbO_3/SiO_2$/Si structure. *IEEE Electron Device Letters, 42*(3), 438–441. https://doi.org/10.1109/LED.2021.3051298.

[12] Zhang, S., Lu, R., Zhou, H., Link, S., Yang, Y., Li, Z., Huang, K., Ou, X., & Gong, S. (2020). Surface acoustic wave devices using lithium niobate on silicon carbide. *IEEE Transactions on Microwave Theory and Techniques, 68*(9), 3653–3666. https://doi.org/10.1109/TMTT.2020.3006294.

[13] Shen, J., Fu, S., Su, R., Xu, H., Lu, Z., Zhang, Q., Zeng, F., Song, C., Wang, W., & Pan, F. (2022). SAW filters with excellent temperature stability and high power handling using $LiTaO_3$/SiC bonded wafers. *Journal of Microelectromechanical Systems, 31*(2), 186–193. https://doi.org/10.1109/JMEMS.2021.3137928.
[14] Bahamonde, J. A., & Kymissis, I. (2020). A reconfigurable surface acoustic wave filter on ZnO/AlGaN/GaN heterostructure. *IEEE Transactions on Electron Devices, 67*(10), 4507–4514. https://doi.org/10.1109/TED.2020.3018697.
[15] Azarnaminy, A. F., Jiang, J., & Mansour, R. R. (2021). Switched dual-band SAW filter using vanadium oxide switches. In *Proceedings of the 2021 IEEE MTT-S International Microwave Symposium (IMS)* (pp. 677–680). Atlanta, GA, USA. https://doi.org/10.1109/IMS19712.2021.9574799.
[16] Yang, Y., Gao, L., & Gong, S. (2021). A miniaturized acoustic dual-band bandpass filter using thin-film lithium niobate. In *Proceedings of the 2021 IEEE International Ultrasonics Symposium (IUS)* (pp. 5–8). Xi'an, China. https://doi.org/10.1109/IUS52206.2021.9593792.
[17] Luo, T., Liu, Y., Zou, Y., Zhou, J., Liu, W., Wu, G., Cai, Y., & Sun, C. (2022). Design and optimization of the dual-mode Lamb wave resonator and dual-passband filter. *Micromachines, 13*(1), 87. https://doi.org/10.3390/mi13010087.
[18] Zou, Y., Nian, L., Cai, Y., Liu, Y., Tovstopyat, A., Liu, W., & Sun, C. (2020). Dual-mode thin film bulk acoustic wave resonator and filter. *Journal of Applied Physics, 128*(19), 194503. https://doi.org/10.1063/5.0028702.
[19] Phani Kumar, K. V., Velidi, V. K., Althuwayb, A. A., & Rama Rao, T. (2021). Microstrip dual-band bandpass filter with wide bandwidth using paper substrate. *IEEE Microwave and Wireless Components Letters, 31*(9), 833–836. https://doi.org/10.1109/LMWC.2021.3077879.
[20] Acosta, L., Guerrero, E., Verdu, J., & de Paco, P. (2022). Topology assessment for dual-band filters based on acoustic wave resonators. *IEEE Transactions on Microwave Theory and Techniques*. (In press). https://doi.org/10.1109/TMTT.2022.3222327.
[21] Campanella, H., Qian, Y., Romero, C. O., Wong, J. S., Giner, J., & Kumar, R. (2021). Monolithic multi-band MEMS RF front-end module for 5G mobile. *Journal of Microelectromechanical Systems, 30*(1), 72–80. https://doi.org/10.1109/JMEMS.2020.3036379.
[22] Liu, Y., Cai, Y., Zhang, Y., Tovstopyat, A., Liu, S., & Sun, C. (2020). Materials, design, and characteristics of bulk acoustic wave resonator: A review. *Micromachines, 11*(7), 630. https://doi.org/10.3390/mi11070630.
[23] Campanella, F., Del Giudice, M., Thrassou, A., & Vrontis, D. (2020). Ambidextrous organizations in the banking sector: An empirical verification of banks' performance and conceptual development. *International Journal of Human Resource Management, 31*(2), 272–302. https://doi.org/10.1080/09585192.2016.1239122.
[24] Khanna, G., & Sharma, N. (2016). Fractal antenna geometries: A review. *International Journal of Computer Applications, 153*(7), 29–32. https://doi.org/10.5120/ijca2016912106.
[25] Babu, S. S., Mourad, A.-H. I., Harib, K. H., & Vijayavenkataraman, S. (2022). Recent developments in the application of machine learning towards accelerated predictive multiscale design and additive manufacturing. *Virtual and Physical Prototyping, 18*(1). https://doi.org/10.1080/17452759.2022.2141653.